Improving mechanical ice protection systems with topology optimization

Alexis Marbœuf[1] · Marc Budinger[2] · Valérie Pommier-Budinger[1] · Valérian Palanque[1,3] · Lokman Bennani[3]

Abstract
In the context of more electrical aircraft, electromechanical de-icing systems provide a low-energy solution to protect aircraft's surfaces from ice buildup. Such systems produce deformation of the protected surface leading to a stress production within the ice and, ultimately, to ice shedding thanks to fracture. However, these systems may show limitations when it comes to completely protect a given surface. Ice delamination is often restricted to a part of the surface and the remaining ice either requires more energy to be removed or is just impossible to remove. In this paper, topology optimization of the substrate covered by ice is thus investigated to increase fracture propagation and ice shedding. For that purpose, an optimization problem, involving the energy release rate but also the mass and the substrate stress, is formulated. The numerical results show how the delamination efficiency of mechanical based ice protection systems can be improved through the topology modification of the substrate.

Keywords Electromechanical de-icing · Topology optimization · Adjoint method · Adhesive fracture · Energy release rate

1 Introduction

Icing has been identified as a severe issue since the beginning of aviation (Leary 2002; Cao et al. 2018). In flight, ice accretion is caused by supercooled droplets suspended in clouds. They impact the aircraft surfaces and freeze. Ice then accumulates on the surface which may lead to an increase of mass, the degradation of aerodynamic performances, or engine damage/flameout due to ice ingestion.

Ice protection systems are then required to ensure aircraft safety (Aircraft Icing Handbook 2000). Chemical, thermal, or mechanical are current strategies for de-icing or anti-icing. The choice is motivated by the application. Huang et al. (2019, Table 1) drew advantages and drawbacks of these possible strategies to ease such a choice. Note that combined solutions also exist (Strobl et al. 2015; Zhang et al. 2017). Electromechanical ice protection systems show a growing interest in the literature in the context of more electrical aircraft. They are especially interesting for their potential in terms of weight, durability, and energy savings. In such systems, electric actuators feed the protected surface with deformations. These deformations generate stress within the ice leading to cohesive (bulk fracture) and adhesive (delamination) failures.

A large amount of work has been carried out to study the efficiency of electromechanical ice protection systems with different types of excitation (static, modal, impulsive,...) ranging from the low frequency range (Hertz) (Venna and Lin 2003, 2006; Venna et al. 2007), the kiloHertz range (Palacios and Smith 2005; Palacios 2008; Palacios et al. 2008, 2011a, b; Overmeyer et al. 2011, 2012; Villeneuve et al. 2015; Strobl et al. 2015), and the megaHertz range (Ramanathan et al. 2000; Kalkowski et al. 2015). In this paper, the focus is put on quasi-static deformation which show close similarity with low-frequency flexural resonant modes. Using beam theory, modal analysis, and numerical tools, Budinger et al. (Budinger et al. 2016; Pommier-Budinger et al. 2018; Budinger et al. 2018, 2021) studied these modes. Although they assumed a priori the fracture

Responsible Editor: Emilio Carlos Nelli Silva

✉ Alexis Marbœuf
alexis.marboeuf@hotmail.fr

[1] ISAE-SUPAERO, Université de Toulouse, Toulouse, France

[2] Institut Clément Ader (ICA), Université de Toulouse, INSA, ISAE-SUPAERO, MINES ALBI, UPS, CNRS, 3 Rue Caroline Aigle, 31400 Toulouse, France

[3] ONERA/DMPE, Université de Toulouse, 31055 Toulouse, France

path leading to ice debonding in their work, Marbœuf et al. gave more weight to this fracture mechanism thanks to a phase-field variational approach for brittle fracture (Marbœuf et al. 2020). Budinger et al. concluded that these low-frequency resonant modes proved to be efficient for cohesive fracture within the ice but failed to shed the ice from the structure. There is then a need to improve the efficiency of such modes, interesting for their low consumption. For that purpose, optimization of the substrate is considered. Palanque et al. (2021) propose a parametric optimization of the substrate thickness based on beam theory and fracture criterion introduced in Budinger et al. (2021). In this paper, topology optimization is explored. This allows to keep a total freedom in shaping the substrate. The delamination efficiency but also the substrate mass and stress are quantities of particular interest.

The paper is organized as follows: (i) literature review on topology optimization for fracture problems; (ii) set-up and the fracture model; (iii) formulation of the topology optimization problem; (iv) sensitivity analysis performed by the adjoint Method; (v) numerical results; and (vi) conclusion.

2 Topology optimization for fracture problems

Topology optimization is widely used for engineering problems with more than 30 years of study. Among the large range of applications, one can find fluid–structure interactions (Akl et al. 2009), vibration control (Zargham et al. 2016), or damage detection (Niemann et al. 2010). Whatever the physical application, material topology has to be represented within the computational domain. Classical techniques for that purpose are homogenization (Nishiwaki et al. 1998), solid isotropic material with penalization (SIMP) (Sigmund 2001; Andreassen et al. 2011), bidirectional evolutionary structural optimization (BESO) (Huang et al. 2010; Huang and Xie 2010), and level-set (Allaire et al. 2004) methods. These techniques consist in defining a density variable $0 \leq \rho \leq 1$ within each computational element of the mesh representing the material presence, except for level-set method where the material is implicitly defined thanks to an isoline of the level-set function. Once the material model is selected, a numerical scheme is applied to solve the optimization problem. The difficulty here is the very large number of optimization variables. Again, the literature provides a large range of suitable techniques such as the gradient-based method of moving asymptotes (MMA) (Svanberg 1987) which is among the best known and used. Zargham et al. summarized these numerical techniques (Zargham et al. 2016).

Fracture was firstly taken into account in topology optimization through stress constraints to prevent crack initiation (Duysinx and Bendsøe 1998; Le et al. 2010). Damage models were also introduced in topology optimization algorithms to obtain optimal shapes of steel reinforcement bars within concrete (Amir 2013). Some authors proposed an explicit fracture propagation algorithm coupled with topology optimization. Kang et al. (2017) improved the fracture resistance of pre-cracked structures using the J-Integral (Sih and Rice 1965) as an objective for topology optimization. Klarbring et al. (2018) successfully minimized the energy released rate, computed with the virtual crack extension (Parks 1974), of fatigue-cracked aeronautics structures by optimizing the shape of reinforcement patches. J-Integral or virtual crack extension techniques usually serve as a criterion to determine if a crack propagates further on specific pre-cracked locations within a material. More complete fracture initiation and propagation models are used to fully simulate the fracture process. These models are coupled with topology optimization at the expense of a drastically increasing computational cost: see Xia et al. (2018); Russ and Waisman (2019) for phase-field variational approaches of fracture and Liu et al. (2016) for an extended finite element method (XFEM). These complete but expensive fracture models can also be partially introduced into J-integral or crack virtual extension techniques. As an example, Waisman (2010) combined XFEM and virtual crack extension techniques to derive an analytical expression for the stiffness derivative with respect to the fracture state. All these techniques were mainly applied on cohesive fracture problems. Many authors also considered adhesive fracture inside a topology optimization algorithm and different methods came into the picture compared to cohesive fracture. Sylves et al. (2009) solved the adhesion problem between two elastic plates starting from a Lennard-Jones function to derive a stress-opening relation at the adhesive interface, which is closely related to Cohesive Zone Model (CZM). Mergel et al. (2014) or Hsueh and Bhattacharya (2018) tackled the peeling problem of a thin film on a substrate. The first authors adopted a microscopic point of view, defining an adhesive energy density based on van der Walls interactions while Hsueh and Bhattacharya modeled the adhesive interface thanks to governing equations of the peeling problem derived in Xia et al. (2015); Dondl and Bhattacharya (2016). Finally, topology optimization problems were also formulated taking into account both adhesive and cohesive fractures and their interactions (Nguyen et al. 2016; Da et al. 2018; Da 2019; Da and Yvonnet 2020).

3 Set-up and fracture model

3.1 Geometry

Two-dimensional plain strain geometries are considered. Figures 1 and 2 display the configurations of this paper, together with applied loads, boundary conditions, and

material's parameters (both elastic and adhesive). An imposed displacement $u_{imp} = 1$ mm is directly applied without any increment. The large scattering of materials' available values in literature is out of the scope of the paper and values of (Marbæuf et al. 2020, Sect. 4) are retained. See, for example, Work and Lian (2018) for a review of ice adhesion on solid substrates. Figure 1 corresponds to a 130-mm-long and 1.5-mm-thick beam. Half of the beam is considered thanks to a symmetry condition on the left boundary. The beam is covered with a 2 mm-thick ice layer on its entire length. Configuration 2 corresponds to a 2.5 mm-thick NACA12 profile. Again, Fig. 2 shows half of the profile thanks to the symmetry condition on the bottom boundary. The ice covers $L_{tot} = 112.2$ mm of the NACA12 profile.

3.2 Assumptions

Adhesive fracture between ice and the substrate is considered brittle and instantaneous as in Marbœuf et al. (2020). The latter implies a quasi-static framework as mentioned in introduction.

In this paper, the fracture path is assumed a priori as in Budinger et al. (2016, 2018, 2021). The fracture initiates at the ice surface, propagates through the ice thickness, and finally causes ice delamination. This fracture mechanism was recovered with the phase-field variational approach (Marbœuf et al. 2020). Arrows in Fig. 1 indicate the fracture path. Right boundary for the ice is left free instead of the symmetry condition to consider the presence of the cohesive fracture through the ice thickness. This fracture mechanism

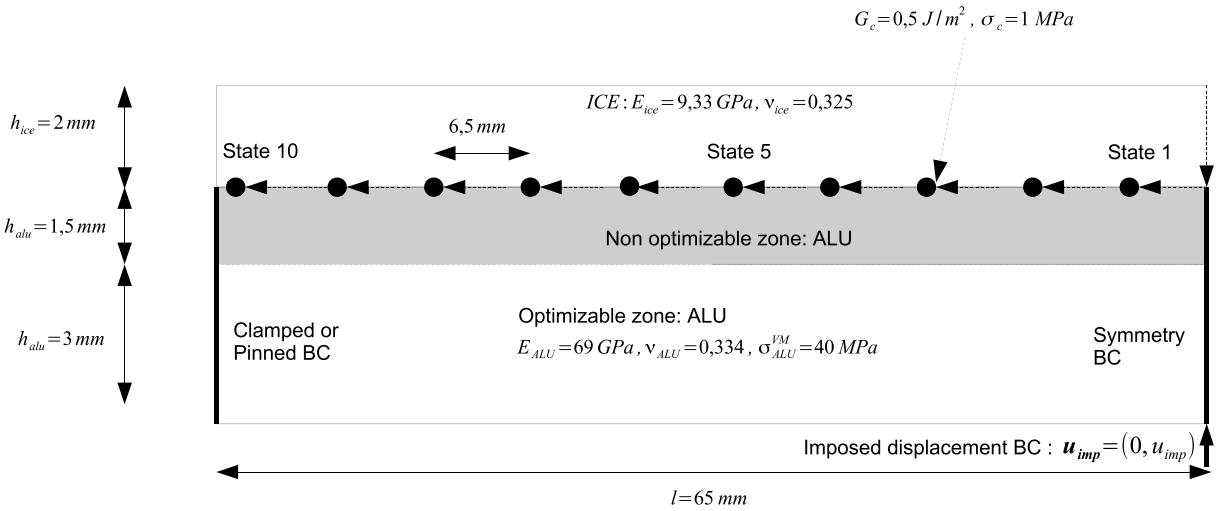

Fig. 1 Configuration 1. Material's parameters are displayed. Each state corresponds to a static FE computation given a fracture delamination length where the energy release rate is computed. Ice covers $L_{tot} = 65$ mm of the half-beam

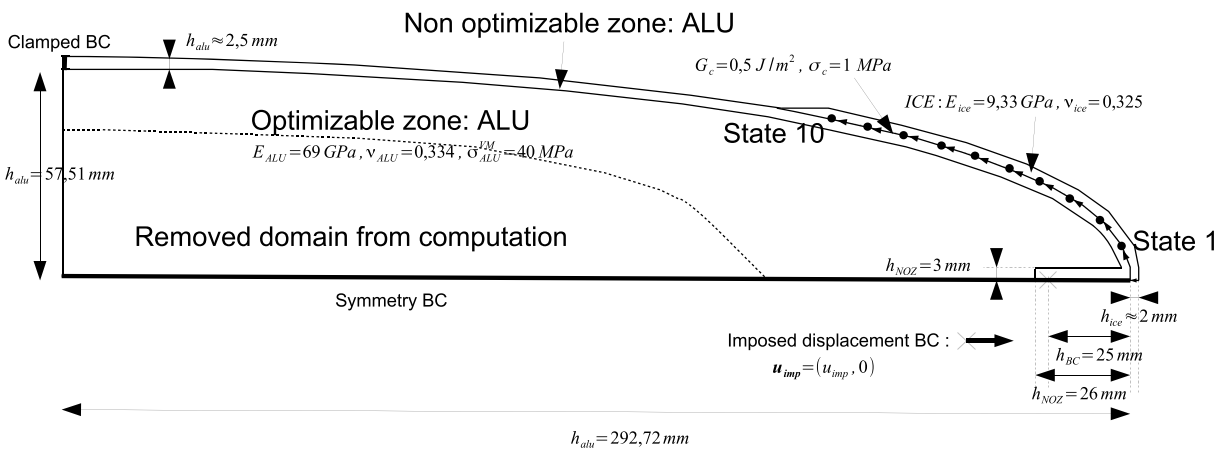

Fig. 2 Configuration 2: NACA12. Material's parameters are displayed. Each state corresponds to a static FE computation given a fracture delamination length where the energy release rate is computed. Ice covers $L_{tot} = 112.2$ mm

is extended to the NACA12 profile of Fig. 2 where arrows represent again the fracture path.

Adhesive interface is discretized into points. Each point corresponds to a state with a given adhesive fracture length, on which a static linear elastic finite element (FE) computation is performed. Figure 1 shows that, for the half-beam of length 65 mm, 10 discretization points are placed on the adhesive interface corresponding to a fracture length propagating every 6.5 mm, leading to 10 different states. For each state, one static elastic FE computation provides the classical fields everywhere on the computational domain: displacement $\boldsymbol{u}$, strain ϵ, stress σ , and elastic energy e.

3.3 Adhesive fracture model

The fracture model is based on the energy release rate introduced by Griffith (1921). He stated that crack propagation is a competition between the elastic energy stored in the bulk of a material and a fracture energy, proportional to the surface's area created by new fractures. In other words, a crack propagates if the energy released during the process is greater or equal to a value proportional to the new surface's area created. The proportional factor is the so-called Griffith critical energy release rate G_c and is a material-dependent parameter. The value $G_c = 0.5\,\mathrm{J/m^2}$ is used in all the numerical results as shown in Figs. 1 and 2.

According to Frémond (1987), elastic microscopic bonds model the adhesive interface in this work as in Bennani et al. (2016); Marbœuf et al. (2020). These elastic microscopic bonds store the energy within the interface. This energy is then available for adhesive fracture. In 2D, the energy release rate thus takes the form of Eq. 1 for a $\delta\ell$ fracture length, which is nothing but the potential energy of the fictitious adhesive springs of stiffnesses k_n and k_τ. The displacement jump $[\![\boldsymbol{u}]\!]$ across the adhesive interface is extracted from the displacement field $\boldsymbol{u}$ over the length $\delta\ell$.

$$G = \frac{1}{\delta\ell}\int_0^{\delta\ell} \frac{1}{2}\left[k_n < [\![\boldsymbol{u}]\!]_n >_+^2 + k_\tau [\![\boldsymbol{u}]\!]_\tau^2\right] d\ell \tag{1}$$

The energy release rate G in Eq. (1) is evaluated at each discretization point on the adhesive interface considering a virtual fracture length of $\delta\ell = 1$ mm. The energy $G\,\delta\ell$ is thus the energy released during a virtual adhesive fracture of $\delta\ell = 1$ mm at the corresponding discretization point. One evaluation of G requires one static FE computation. Mode I and Mode II failures are taken into account through the decoupling of the displacement jump $[\![\boldsymbol{u}]\!]$ across the interface into two components: normal $[\![\boldsymbol{u}]\!]_n$ and tangential $[\![\boldsymbol{u}]\!]_\tau$ components. Eq. 1 involves only the positive part $< . >_+$ of the normal displacement jump $[\![\boldsymbol{u}]\!]_n$, meaning that only the normal traction participates to adhesive fracture Miehe et al. (2010). Figure 3 shows the adhesive interface model used in this paper. The normal stiffness k_n is deduced from more common interface values available in literature thanks to a pure traction test: the critical stress σ_c and the adhesive critical energy release rate G_c. The values $G_c = 0.5\,\mathrm{J/m^2}$ and $\sigma_c = 1$ MPa lead to $k_n = 9.48 \times 10^{12}$ Pa/m (Marbœuf et al. 2020, Sect. 4). The tangential stiffness k_τ is taken such that Mode II contribution is divided by 10 compared to Mode I (Marbœuf et al. 2020, Sect. 4), i.e., $k_\tau = k_n/10$. No additional adhesive model is included. In particular, no contact are applied and inter-penetration is not forbidden.

This approach shares some similarities or links with existing techniques described in the previous section: (i) a virtual move of a computational node mimicks a virtual fracture in the virtual crack extension; (ii) the density energy in Eq. 1 corresponds to a part of the adhesive elastic energy used in the phase-field variational approach of Bennani et al. (2016); Marbœuf et al. (2020); (iii) the traction-separation law of CZM can be derived from the complete adhesive elastic energy density under some assumptions (Wu 2017; Wu and Nguyen 2018; Marbœuf et al. 2020); and (iv) the complete fictitious energy density of Bennani et al. (2016); Marbœuf et al. (2020) simplifies and renders more complex microscopic interactions such as van der Walls interactions. The reader is referred to Wu (2017); Wu and Nguyen (2018) for further details on point (iii).

3.4 Fracture criteria

Based on energy release rates G_i along the adhesive interface, two criteria are introduced to represent the adhesive fracture mechanism.

A first criterion sorts all energy release rates $G_0 > G_1 > ... > G_N$ along the adhesive interface

$$\frac{G_{i+1} - G_i}{G_i} \leq \delta G_c, \quad i = 0, \ldots, N-1, \tag{2}$$

where N is the last state number on the fixed protected length. Inequality (2) imposes a maximum slope of 5 %

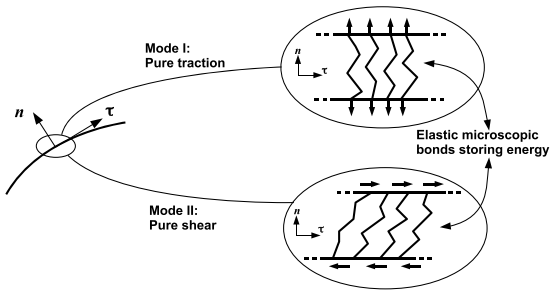

Fig. 3 Adhesive microscopic bonds modeling the adhesive interface. These bonds store energy which is released during the fracture process. Both Mode I and II are taken into account

locally with $\delta G_c = -0.05$. Criterion (2) provides a simple way to control fracture initiation along the adhesive interface. When the criterion (2) is met, the interface energy stored locally at each discretization point decreases with the length of the adhesive fracture. The criterion *a priori* implies that the local stress on the adhesive interface also decreases with the fracture length, avoiding unwanted fracture initiation, except at the considered discretization point. The idea behind that criterion is thus to enforce the assumed fracture path. Note that criterion (2) is limited to local areas around discretization points and fracture initiations elsewhere on the adhesive interface is uncontrolled. For computational considerations, the energy release rate replaces the stress in (2). The stress needs very fine meshes to be well resolved, in particular when only local values on discretization points are of interest. Finally, criterion (2) does not consider cohesive fracture initiation within the ice. The last point will be explored in the numerical results.

The second criterion writes (Budinger et al. 2021)

$$\frac{G_c}{\left(\sigma_c^{VM}\right)^2} \leq \frac{G_N}{\left(\sigma_N^{VM}\right)^2} \tag{3}$$

where σ_N^{VM} denotes the maximum Von-Mises stress within the substrate at the state N and σ_c^{VM} is the critical Von-Mises stress. The criterion (3) combines the two inequalities $G_c \leq G_N$ and $\sigma_N^{VM} \leq \sigma_c^{VM}$. Both bounds G_c and σ_c^{VM} depend on the applied displacement amplitude. Martin et al. (2016) showed by dimensional analysis that the quantity G/σ^2 is both representative of the fracturing mechanism and independent of the displacement amplitude. The quantity G/σ^2 is therefore more easily boundable. While no damage model is taken into account in the substrate, the criterion (3) allows to control the stress within the substrate: it undergoes bounded Von-Mises stresses

$$\sigma_N^{VM} \leq \sqrt{\frac{G_N}{G_c}}\sigma_c^{VM}.$$

4 Optimization problem

The material is described in this paper with a modified SIMP approach (Sigmund 2001; Andreassen et al. 2011). In each element cell c, Young's modulus E_c and stress σ_c are degrading according to the material presence ρ_c

$$E_c = E_{min} + \rho_c^p\left(E_{mat} - E_{min}\right) \tag{4}$$

$$\sigma_c = \rho_c^q\,\sigma_{mat} \tag{5}$$

where E_{mat} is the material Young's modulus, $E_{min} = 10^{-4}$ allows keeping an invertible stiffness matrix, $p = 3$ and $q = 1.5$ are penalization parameters. The parameter p allows a more black & white solution (Andreassen et al. 2011) while q is a numerical parameter to ease the convergence (Holmberg et al. 2013).

Given the set-up introduced in the previous section, the optimization problem is formulated as follows:

$$\begin{aligned} &\min_{\boldsymbol{\rho}} \quad \frac{m^r}{G_N^s} \\ &\text{submitted to:} \begin{cases} \frac{G_{i+1}-G_i}{G_i} \leq \delta G_c \quad i = 0, ..., N \\ \frac{G_c}{\left(\sigma_c^{VM}\right)^2} \leq \frac{G_N}{\left(\sigma_N^{VM}\right)^2} \\ 0 \leq \boldsymbol{\rho} \leq 1 \end{cases} \end{aligned} \tag{6}$$

where $\boldsymbol{\rho} = (\rho_c)^t$ is the collection of all design variables, m is the mass proportion and i denotes the state number. The objective is weighted thanks to parameters $r = 2$ and $s = 1$. A few tests were run with different combinations of r and s and it shows that the mass should be more weighted in order to obtain sufficiently light structures. Moreover, a large value of r is useless and values given here seem to be a good compromise.

The optimization problem (6) allows minimizing the mass proportion while maximizing the last energy release rate G_N of the protected zone. The two first constraints in (6) are described in the previous section and control the fracture mechanism. Problem (6) is now solved using classical existing techniques in literature. A smoothing filter (Andreassen et al. 2011; Lazarov and Sigmund 2011) reduces mesh-dependency and improves convergence. The length parameter $R = 5.0$ is chosen in numerical results leading to a smoothing over approximately 5 cells. No Black and White filter (Andreassen et al. 2011; Russ and Waisman 2019) is used to remove intermediate values $0 < \boldsymbol{\rho} < 1$. The first constraint in problem (6) proves to be very sensitive to a Black & White filter. Removing intermediate densities, unavoidable because of the first smoothing filter, at specific locations, often violates the constraint $\frac{G_{i+1}-G_i}{G_i} \leq \delta G_c$. This will be further discussed with the numerical results. The maximum Von-Mises stress within the substrate at the State N σ_N^{VM} is approximated thanks to an aggregate function depending on all local stresses in each element of the mesh. The discrete L^k-norm where $k = 4$ is used as the aggregate function. The approximation is improved thanks to the clustering-based approach of Holmberg et al. (2013). Stresses values are sorted into 3 clusters from the lower to the higher value. Finally, MMA (Svanberg 1987) solves the problem (6). As it is stated before, it is a widely used method for topology optimization since it can handle an arbitrary number of non-linear constraints. However, it requires the computation of gradients with respect to design variables ρ_c

which is detailed in the following section. Figure 4 displays the flowchart of the topology optimization algorithm.

5 Sensitivity analysis

Sensitivities with respect to design variables ρ_c required by MMA are computed with the adjoint method: see Russ and Waisman (2019); Holmberg et al. (2013) for an example of adjoint sensitivity computations.

Let $\boldsymbol{U} = (\boldsymbol{u}_p)^t$ the displacement vector for all computational nodes p and $\mathcal{J}_s$ the operator such that $[\![\boldsymbol{u}]\!]_s = \mathcal{J}_s \boldsymbol{U}$ for each discrete segment s of the adhesive interface. The vector $\boldsymbol{n}_s$ (resp. $\boldsymbol{\tau}_s$) denotes the normal (resp. tangential) vector of segment s and is function of $\boldsymbol{U}$. In this section, the state number is dropped for the sake of clarity. The discretized form of Eq. (1) writes

$$G = \frac{1}{\delta\ell} \sum_s \tfrac{1}{2} \Big[k_n \big[\delta_+(\boldsymbol{n}_s^t \mathcal{J}_s \boldsymbol{U})\big]^2 + k_\tau \big[\boldsymbol{\tau}_s^t \mathcal{J}_s \boldsymbol{U}\big]^2 \Big] \tag{7}$$

where δ_+ is a regularized function approximated the positive part $< . >_+$. That function is given by

$$\delta_+(x) = \frac{1}{2}(1 + tanh(\eta\, x))\, x$$

with $\eta = 5 \times 10^4$ a user-defined parameter controlling the regularization length around zero. Partial derivation of G with respect to a design variable ρ_c yields

$$\begin{aligned} \frac{\partial G}{\partial \rho_c} &= \frac{1}{\delta\ell} \sum_s \tfrac{1}{2} \Big[k_n \frac{\partial}{\partial \rho_c} \big[\delta_+(\boldsymbol{n}_s^t \mathcal{J}_s \boldsymbol{U})\big]^2 + k_\tau \frac{\partial}{\partial \rho_c} \big[\boldsymbol{\tau}_s^t \mathcal{J}_s \boldsymbol{U} \cdot\big]^2 \Big] \\ &= \frac{1}{\delta\ell} \sum_s \Big[k_n\, \delta_+(\boldsymbol{n}_s^t \mathcal{J}_s \boldsymbol{U}) \frac{\partial \delta_+(\boldsymbol{n}_s^t \mathcal{J}_s \boldsymbol{U})}{\partial \rho_c} + k_\tau\, \boldsymbol{\tau}_s^t \mathcal{J}_s \boldsymbol{U} \frac{\partial (\boldsymbol{\tau}_s^t \mathcal{J}_s \boldsymbol{U})}{\partial \rho_c} \Big] \end{aligned}$$

One gets

$$\begin{aligned} \frac{\partial \delta_+(\boldsymbol{n}_s^t \mathcal{J}_s \boldsymbol{U})}{\partial \rho_c} &= \delta'_+(\boldsymbol{n}_s^t \mathcal{J}_s \boldsymbol{U}) \frac{\partial (\boldsymbol{n}_s^t \mathcal{J}_s \boldsymbol{U})}{\partial \rho_c} \\ &= \delta'_+(\boldsymbol{n}_s^t \mathcal{J}_s \boldsymbol{U}) \Big[\Big(\frac{\partial \boldsymbol{n}_s}{\partial \rho_c} \Big)^t \mathcal{J}_s \boldsymbol{U} + \boldsymbol{n}_s^t \mathcal{J}_s \frac{\partial \boldsymbol{U}}{\partial \rho_c} \Big] \\ &= \delta'_+(\boldsymbol{n}_s^t \mathcal{J}_s \boldsymbol{U}) \Big[\boldsymbol{U}^t \mathcal{J}_s^t \frac{\partial \boldsymbol{n}_s}{\partial \boldsymbol{U}} + \boldsymbol{n}_s^t \mathcal{J}_s \Big] \frac{\partial \boldsymbol{U}}{\partial \rho_c} \end{aligned}$$

The partial derivative $\frac{\partial \boldsymbol{\tau}_s}{\partial \rho_c}$ follows from the same calculation

$$\frac{\partial \boldsymbol{\tau}_s}{\partial \rho_c} = \Big[\boldsymbol{U}^t \mathcal{J}_s^t \frac{\partial \boldsymbol{\tau}_s}{\partial \boldsymbol{U}} + \boldsymbol{\tau}_s^t \mathcal{J}_s \Big] \frac{\partial \boldsymbol{U}}{\partial \rho_c}.$$

Eq. (7) now becomes

$$\begin{aligned} \frac{\partial G}{\partial \rho_c} = \frac{1}{\delta\ell} \sum_s \Big[& k_n\, \delta_+(\boldsymbol{n}_s^t \mathcal{J}_s \boldsymbol{U}) \delta'_+(\boldsymbol{n}_s^t \mathcal{J}_s \boldsymbol{U}) \big[\boldsymbol{U}^t \mathcal{J}_s^t \frac{\partial \boldsymbol{n}_s}{\partial \boldsymbol{U}} + \boldsymbol{n}_s^t \mathcal{J}_s \big] \\ & + k_\tau\, \boldsymbol{\tau}_s^t \mathcal{J}_s \boldsymbol{U} \big[\boldsymbol{U}^t \mathcal{J}_s^t \frac{\partial \boldsymbol{\tau}_s}{\partial \boldsymbol{U}} + \boldsymbol{\tau}_s^t \mathcal{J}_s \big] \Big] \frac{\partial \boldsymbol{U}}{\partial \rho_c}. \end{aligned} \tag{8}$$

The adjoint method allows an efficient computation of (8). An adjoint variable λ_1

$$\begin{aligned} \lambda_1^t = \frac{1}{\delta\ell} \sum_s \Big[& k_n\, \delta_+(\boldsymbol{n}_s^t \mathcal{J}_s \boldsymbol{U}) \delta'_+(\boldsymbol{n}_s^t \mathcal{J}_s \boldsymbol{U}) \big[\boldsymbol{U}^t \mathcal{J}_s^t \frac{\partial \boldsymbol{n}_s}{\partial \boldsymbol{U}} + \boldsymbol{n}_s^t \mathcal{J}_s \big] \\ & + k_\tau\, \boldsymbol{\tau}_s^t \mathcal{J}_s \boldsymbol{U} \big[\boldsymbol{U}^t \mathcal{J}_s^t \frac{\partial \boldsymbol{\tau}_s}{\partial \boldsymbol{U}} + \boldsymbol{\tau}_s^t \mathcal{J}_s \big] \Big] \boldsymbol{K}^{-1} \end{aligned}$$

is first computed with

$$\begin{aligned} \boldsymbol{K}\lambda_1 = \frac{1}{\delta\ell} \sum_s \Big[& k_n\, \delta_+(\boldsymbol{n}_s^t \mathcal{J}_s \boldsymbol{U}) \delta'_+(\boldsymbol{n}_s^t \mathcal{J}_s \boldsymbol{U}) \big[\Big(\frac{\partial \boldsymbol{n}_s}{\partial \boldsymbol{U}} \Big)^t \mathcal{J}_s \boldsymbol{U} + \mathcal{J}_s^t \boldsymbol{n}_s \big] \\ & + k_\tau\, \boldsymbol{\tau}_s^t \mathcal{J}_s \boldsymbol{U} \big[\Big(\frac{\partial \boldsymbol{\tau}_s}{\partial \boldsymbol{U}} \Big)^t \mathcal{J}_s \boldsymbol{U} + \mathcal{J}_s^t \boldsymbol{\tau}_s \big] \Big] \end{aligned}$$

where $\boldsymbol{K}$ is the FE stiffness matrix. With the adjoint variable, Eq. (8) writes

$$\frac{\partial G}{\partial \rho_c} = -\lambda_1^t \frac{\partial \boldsymbol{K}}{\partial \rho_c} \boldsymbol{U}. \tag{9}$$

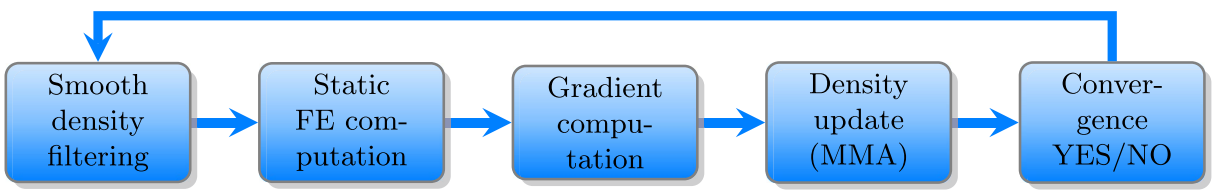

Fig. 4 Flowchart of the topology optimization algorithm

Note that $\frac{\partial \boldsymbol{n}_s}{\partial \boldsymbol{U}}$ and $\frac{\partial \boldsymbol{\tau}_s}{\partial \boldsymbol{U}}$ are easily computed since normal and tangential vectors $\boldsymbol{n}_s$ and $\boldsymbol{\tau}_s$ are simple expressions of the node displacements of the segment s.

Moving on the Von-Mises stress derivative, one follows the same procedure of Holmberg et al. (2013). Recalling that the discrete L^k-norm is used as an aggregate function, the discrete maximum Von-Mises stress in cluster number j is

$$\sigma_j^{VM} = \left[\frac{1}{N_{\mathbb{S}_j}} \sum_{e \in \mathbb{S}_j} \left(\sigma_e^{VM}\right)^k \right]^{1/k}$$

where $\mathbb{S}_j$ is the set of all computational cells in the cluster j and $N_{\mathbb{S}_j}$ its cardinal. Using the chain rule, one has

$$\frac{\partial \sigma_j^{VM}}{\partial \rho_c} = \sum_{e \in \mathbb{S}_j} \frac{\partial \sigma_j^{VM}}{\partial \sigma_e^{VM}} \left(\frac{\partial \sigma_e^{VM}}{\partial \boldsymbol{\sigma}_e} \right)^t \frac{\partial \boldsymbol{\sigma}_e}{\partial \rho_c}$$

where $\boldsymbol{\sigma}_e = (\sigma_e^{11}\ \sigma_e^{22}\ \sigma_e^{33}\ \sigma_e^{21})^t$ in Voigt notation for 2D plain strain geometry. Expressing the stress $\boldsymbol{\sigma}_e$ in the cell e under the form $\boldsymbol{\sigma}_e = \mathbb{C}_e \mathbb{B}_e \boldsymbol{U}$ with $\mathbb{C}_e$ the element constitutive matrix and $\mathbb{B}_e$ the element strain-displacement matrix, the relation becomes

$$\begin{aligned} \frac{\partial \sigma_j^{VM}}{\partial \rho_c} = & \sum_{e \in \mathbb{S}_j} \frac{\partial \sigma_j^{VM}}{\partial \sigma_e^{VM}} \left(\frac{\partial \sigma_e^{VM}}{\partial \boldsymbol{\sigma}_e} \right)^t \frac{\partial \mathbb{C}_e}{\partial \rho_c} \mathbb{B}_e \boldsymbol{U} \\ & + \sum_{e \in \mathbb{S}_j} \frac{\partial \sigma_j^{VM}}{\partial \sigma_e^{VM}} \left(\frac{\partial \sigma_e^{VM}}{\partial \boldsymbol{\sigma}_e} \right)^t \mathbb{C}_e \mathbb{B}_e \frac{\partial \boldsymbol{U}}{\partial \rho_c} \end{aligned}$$

An adjoint variable λ_2^j is now defined according to

$$(\lambda_2^j)^t = \sum_{e \in \mathbb{S}_j} \frac{\partial \sigma_j^{VM}}{\partial \sigma_e^{VM}} \left(\frac{\partial \sigma_e^{VM}}{\partial \boldsymbol{\sigma}_e} \right)^t \mathbb{C}_e \mathbb{B}_e \boldsymbol{K}^{-1}$$

The adjoint variable is computed by solving

$$\boldsymbol{K} \lambda_2^j = \sum_{e \in \mathbb{S}_j} \frac{\partial \sigma_j^{VM}}{\partial \sigma_e^{VM}} \mathbb{B}_e^t \mathbb{C}_e^t \frac{\partial \sigma_e^{VM}}{\partial \boldsymbol{\sigma}_e}.$$

Finally, the sensitivity of σ_j^{VM} is obtained.

$$\begin{aligned} \frac{\partial \sigma_j^{VM}}{\partial \rho_c} = & \sum_{e \in \mathbb{S}_j} \frac{\partial \sigma_j^{VM}}{\partial \sigma_e^{VM}} \left(\frac{\partial \sigma_e^{VM}}{\partial \boldsymbol{\sigma}_e} \right)^t \frac{\partial \mathbb{C}_e}{\partial \rho_c} \mathbb{B}_e \boldsymbol{U} \\ & - (\lambda_2^j)^t \frac{\partial \boldsymbol{K}}{\partial \rho_c} \boldsymbol{U}. \end{aligned} \tag{10}$$

Again, all the partial derivatives $\frac{\partial \sigma_j^{VM}}{\partial \sigma_e^{VM}}$, $\frac{\partial \sigma_e^{VM}}{\partial \boldsymbol{\sigma}_e}$, and $\frac{\partial \mathbb{C}_e}{\partial \rho_c}$ are deduced from the simple expressions of, respectively, σ_j^{VM}, σ_e^{VM}, and $\mathbb{C}_e$. The reader can refer to Holmberg et al. (2013) for further details.

Sensitivity computations are checked with a first-order finite difference computation on 20 cells randomly picked up inside the optimizable domain. More precisely, the following relation

$$\frac{\partial f}{\partial \rho_c}(\boldsymbol{\rho}) - \frac{f(\boldsymbol{\rho}_\Delta) - f(\boldsymbol{\rho})}{\Delta \rho} = \mathcal{O}(\Delta \rho)$$

is checked for each random cell c, where $\boldsymbol{\rho} = (\rho_0, \cdots, \rho_c, \cdots, \rho_{dim})$ is a design variable state, $\boldsymbol{\rho}_\Delta = (\rho_0, \ldots, \rho_c + \Delta\rho, \ldots, \rho_{dim})$, dim the number of design variables, and $\Delta\rho$ a small parameter going to zero.

6 Numerical results

All test cases performed on this paper are summarized in Table 1. A reference configuration of the substrate serves as a comparison on every test cases. In particular, the improved performance of the optimized design is deduced by analyzing the criterion G/σ^2 with respect to the reference. This reference configuration corresponds to a uniform substrate of 1.5 mm for Configuration 1 and approximately 2.5 mm for Configuration 2, *i.e.*, $\boldsymbol{\rho} = 0$ is taken as a reference for all configurations. A classical stiffness optimization problem

$$\begin{aligned} & \max_{\boldsymbol{\rho}} \quad \left(\boldsymbol{u}^t \boldsymbol{K} \boldsymbol{u}\right)_N \\ & \text{submitted to:} \begin{cases} m \leq m_c \\ 0 \leq \boldsymbol{\rho} \leq 1 \end{cases} \end{aligned} \tag{11}$$

also serves as a comparison for Cases 1 and 2. Note that only the overall stiffness of the structure at the state N is maximized. The mass constraint m_c is set according to the optimized result of problem (6) in order to have the same amount of mass. Initial designs are $\boldsymbol{\rho} = 1$ or $\boldsymbol{\rho} = 0.5$ depending on the numerical convergence. The Von-Mises critical stress σ_c^{VM}, involved in the second constraint of problem (6), is taken to 40 MPa. The optimal design often results in a strict inequality $G_c/(\sigma_c^{VM})^2 < G_N/(\sigma_N^{VM})^2$. An effective stress is then defined as $\sigma_T = \sqrt{\frac{G_c}{G_N}} \sigma_N^{VM}$ and that value will be given for each test case. Cases 1, 2, and 3 are computed on the finer possible mesh according to the current limitations of the code, *i.e.*, a mesh around 620000 cells.

6.1 Cases 1 and 2

Figures 5(top) and 6(top), respectively, show the optimal design for Cases 1 and 2. Both designs are similar. The optimal structure can be viewed as a sandwich structure with a maximum 4.5 mm thickness. The structure is composed of two skins with reinforcement bars. Most of the material between the two skins is removed in order to light as

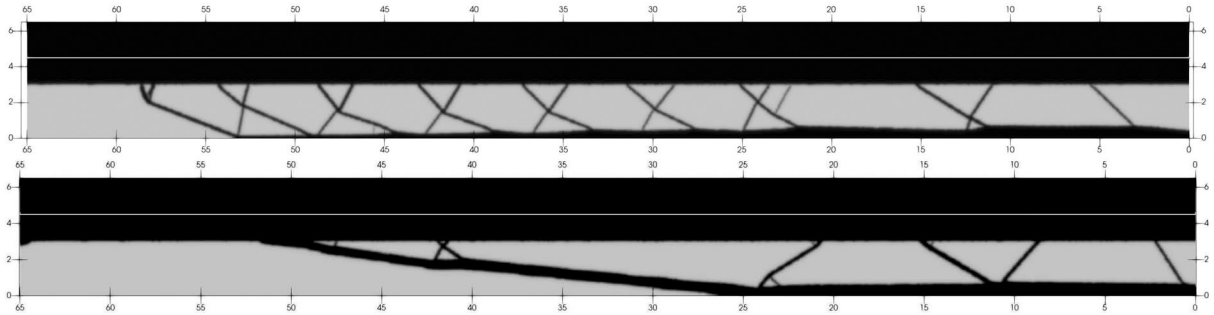

Fig. 5 Case 1: (top) optimized design of problem (6); and (bottom) stiffness optimized design of problem (11). Designs are obtained for the pinned boundary condition in configuration 1. Blank line separates the ice from the substrate. Delamination occurs: (top) on the protected length, *i.e.*, on 90 % (Table 1) of the total length covered by ice; and (bottom) on 82 % of the total length covered by ice

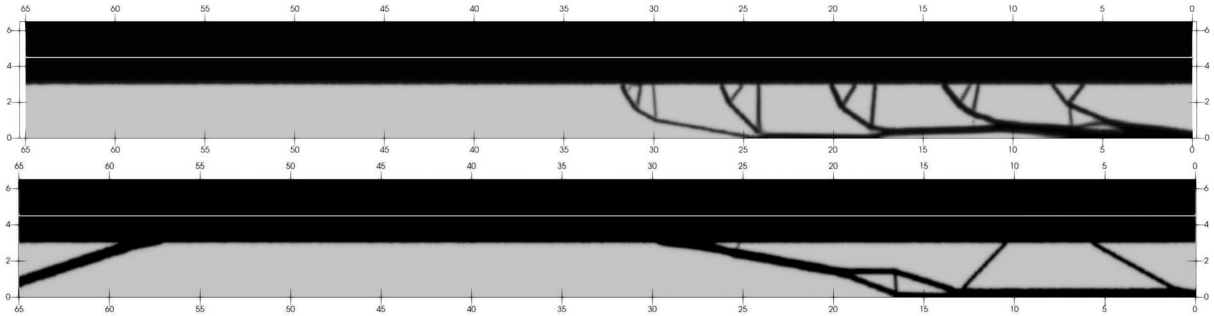

Fig. 6 Case 2: (top) optimized design of problem (6); (bottom) stiffness optimized design of problem (11). Designs are obtained for the clamped boundary condition in configuration 1. Blank line separates the ice from the substrate. Delamination occurs: (top) on the protected length, *i.e.*, on 50 % (Table 1) of the total length covered by ice, and (bottom) on 0 % of the total length covered by ice

much as possible the structure. The first skin corresponds to the non-optimizable area of 1.5 mm thickness. The second skin is less thick and presents a decreasing thickness when moving away from the center of the beam. Hence, the overall stiffness of the structure also decreases and consequently the energy release rate along the adhesive interface in accordance with the first constraint in problem (6). Topology optimization allows here to keep the same delamination performance with much lighter structures compared to a thickness parametric optimization (Palanque et al. 2021) where the structure is full. In the truss-shaped structure, the reinforcement bars keep the two skins bonded and resist to normal (with respect to the interface) compression and shear deformations but allow tangential deformations coming from flexion. It seems that these bars are mainly placed at discretization point locations on the adhesive interface. The stiffness at these specific locations is locally increased to maintain a minimum energy release rate level. The result thus depends on the discretization performed. It is particularly visible on Figure 6(top). Computations were run with more discretization points and show that the material between the two skins is rearranged differently and more reinforcement bars are added. No particular structure appears with that increase of discretization points but it seems that a truss structure, with a sufficient number of reinforcement bars, or a honeycomb-like structure would do a perfect job. Note that topology optimization adds the second skin on the bottom boundary of the optimizable domain. It would be interesting to change boundaries of the optimizable zone to determine if it gives more optimal results. The classical stiffness topology optimization problem (11) leads to similar designs as it is shown in Figures 5(bottom) and 6(bottom). However, less reinforcement bars are present for the benefit of thicker skins. The truss structure (or honeycomb-like structure) thus seems to disappear: the stiffness topology optimization problem (11) only takes into account the overall stiffness of the structure at the state N and does not constrain the other states. This confirms that a truss or honeycomb-like structure in the optimized designs aims at controlling the fracture mechanism all along the adhesive interface.

Figure 7 displays the Von-Mises stress for the optimal design of Case 2. The stress within the ice is particularly interesting. Stress peaks appear at the ice surface between 15 and 35 mm. A high stress zone is also located on the ice left boundary. These high stress values could be the locations of cohesive fracture initiations. This illustrates one limitation

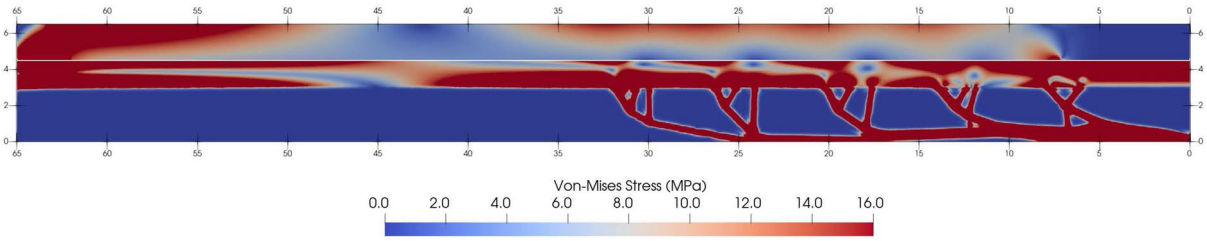

Fig. 7 Case 2: rescaled Von-Mises stress for state 0. Design is obtained with problem (6) for the clamped boundary condition in configuration 1. Blank line separates the ice from the substrate

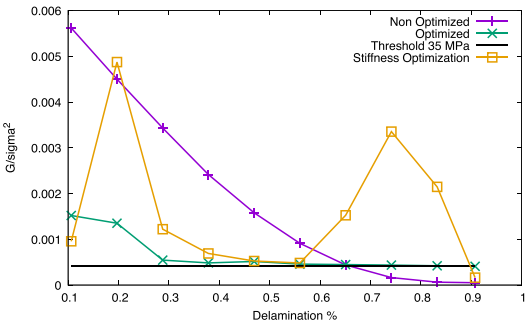

Fig. 8 Case 1: criteria $G_i/(\sigma_i^{VM})^2$ along the adhesive interface for the pinned boundary condition of configuration 1

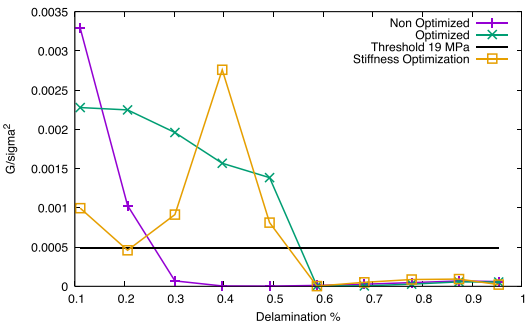

Fig. 9 Case 2: criteria $G_i/(\sigma_i^{VM})^2$ along the adhesive interface for the clamped boundary condition of configuration 1

of the first constraint (2): it does not control stresses within the ice but only local stresses around discretization points on the adhesive interface.

Table 2 sums up the comparison with the reference configuration. In particular, the delamination improvement is given together with the added mass after optimization. Figures 8 and 9 present the criteria $G_i/(\sigma_i^{VM})^2$ along the adhesive interface. It is recalled that a value under the threshold means the adhesive fracture cannot propagate without damaging the substrate. The adhesive fracture propagates with an effective limit for the Von-Mises stress in the substrate around $\sigma_T = 35$ MPa for the Case 1 (pinned boundary condition) and $\sigma_T = 19$ MPa for the Case 2 (clamped boundary

Table 1 Test cases performed in this paper. N_a denotes the number of discretization points on the adhesive interface. L_a is the fixed protected length. It is recalled that ice covers $L_{tot} = 65$ mm of the half-beam for Cases 1 and 2, and $L_{tot} = 112.2$ mm for Case 3

	Figure	Mat.	N_a	BC	L_a/L_{tot} (%)
Case 1	1	Alu	10	Pinned	90
Case 2	1	Alu	10	Clamped	50
Case 3	2	Alu	10	Clamped	90

Table 2 Summary of Cases 1 and 2 for topology optimization problems (6) and (11). Ref values correspond to a uniform substrate of 1.5 mm

	$\frac{m}{m^{ref}}$	$\frac{(G/\sigma^2)_N}{(G/\sigma^2)_N^{ref}}$	σ_T	$\frac{L}{L^{ref}}$
Case 1: (6)	1.38	8.2	35 MPa	1.37
Case 1: (11)	1.38	3.22	35 MPa	1.26
Case 2: (6)	1.24	772.4	19 MPa	2.5
Case 2: (11)	1.24	448.5	19 MPa	0

Exponent *VM* is dropped on the stress σ for more clarity. σ_T is the threshold stress value used in Figs. 8 and 9. L is the optimized delamination length determined thanks to the ratio G/σ^2

condition). The propagation length reaches the goal given in Table 1, *i.e.*, 90 % for Case 1 and 50 % for Case 2. Regarding the reference configuration, the optimization improves the delamination by 37 % and 250 % while adding 38 % and 24 % of mass for, respectively, Cases 1 and 2. Unsurprisingly, the gain is thus much better for the clamped boundary condition. Both for Cases 1 and 2, optimized designs obtained by the problem (11) show less efficiency than the ones from problem (6) in terms of the delamination length, with the same amount of added mass. Keeping the same effective stress $\sigma_T = 19$ MPa, problem (11) even leads to an optimal design with no ice delamination for Case 2: see Table 2. The effective stress should be increased to $\sigma_T = 33$ MPa to recover the same delamination length obtained with problem (6), *i.e.*, a 250 % improvement compared to the reference configuration. Peaks on the quantity G/σ^2 also appear for the stiffness

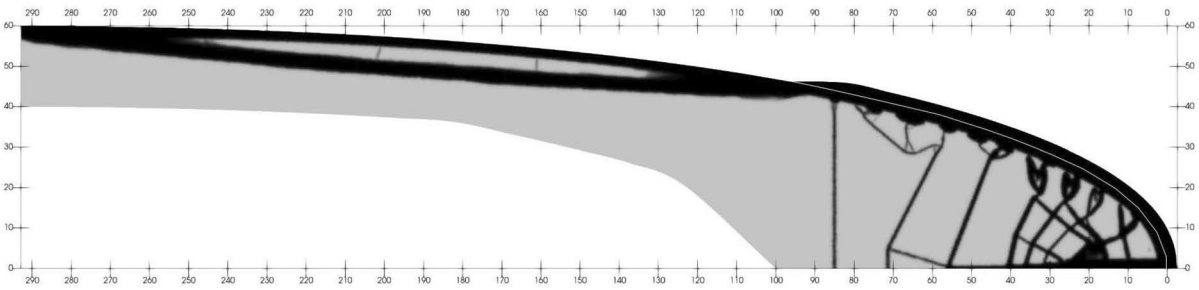

Fig. 10 Case 3: Aluminum optimized design for configuration 2. Blank line separates the ice from the substrate. Delamination occurs on the protected length, i.e., on 90 % (Table 1) of the total length covering by ice

Table 3 Summary of Case 3. Ref values correspond to a uniform substrate of 2.5 mm. Exponent *VM* is dropped on the stress σ for more clarity. σ_T is the threshold stress value used in Fig. 11. L is the optimized delamination length determined thanks to the ratio G/σ^2

	$\frac{m}{m^{ref}}$	$\frac{(G/\sigma^2)_N}{(G/\sigma^2)_N^{ref}}$	σ_T	$\frac{L}{L^{ref}}$
Case 3	2.87	104.3	16 MPa	4.0

optimized designs in Figs. 8 and 9. The first constraint (2) of problem (6) is clearly not fullfilled in that case. These peaks correspond to much higher local values of G, and possibly much higher local stresses, on the adhesive interface and could lead to unwanted adhesive fracture initiations.

Cases 1 and 2 are also performed with an applied displacement amplitude of $u_{imp} = 2$ mm instead of $u_{imp} = 1$ mm. Very similar optimal results are obtained showing that problem (6) is not sensitive to the applied displacement amplitude.

6.2 Case 3

Optimized design is shown in Fig. 10. The optimal shapes share many similarities with Cases 1 and 2: (i) a main bar is added at the symmetry boundary condition playing the role of the second skin; and (ii) a spider web-like structure is placed between the two skins to mimick the truss or honeycomb-like structure. Reinforcements complete the optimal structure when the ice does not cover the substrate anymore. Its goal is twofold: (i) reducing the stress concentration in the substrate where the ice disappears and (ii) reducing stress concentration peaks at the clamped boundary condition.

Criteria $G_i/(\sigma_i^{VM})^2$ plotted in Fig. 11 give a 400 % improvement of the delamination length compared to the reference design with a added mass of 287% as described in Table 3.

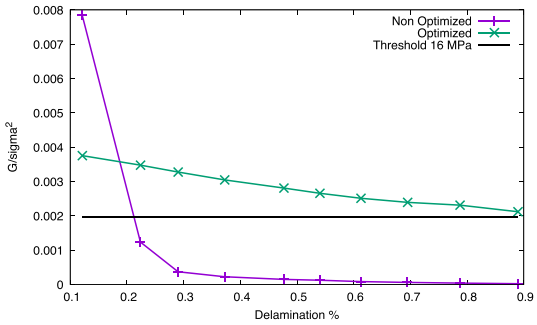

Fig. 11 Case 3: criteria $G_i/(\sigma_i^{VM})^2$ along the adhesive interface for aluminum in configuration 2

7 Conclusion

This paper presents a topology optimization problem for maximizing the delamination efficiency in the context of electromechanical ice protection systems. The optimization problem is formulated in a quasi-static framework and based on energy release rates computed thanks to a novel approach inspired by Bennani et al. (2016); Marbœuf et al. (2020). The mass and the maximum Von-Mises stress within the substrate are also considered in the problem. Three different configurations are tested to gradually improve the geometry complexity from the beam to a realistic NACA12 configuration. These results show that topology optimization successfully increases the delamination efficiency compared to simple reference designs. An improvement of 400 % is even reached on the NACA12 configuration.

Ongoing work includes many possible improvements. First of all, it would be interesting to run more tests modifying parameters. Numerical parameters such as the stress penalization parameter q, the smooth filter parameter R or geometrical parameters such as the thickness of the optimizable zone are worth investigating. Then, the method can be improved in many ways. Parallelization and optimization of the code should be done to run tests with finer meshes. The code is currently limited to meshes around 620000 cells,

considered for all test cases in this paper. Reformulation of the first constraint (2) in problem (6) is needed to avoid a large number of constraints when increasing the number of discretization points. That first constraint (2) also has to be improved for enforcing the fracture path. In particular, the stress within the ice should be taken into account. Finally, modal analysis should replace the quasi-static assumption in the topology optimization problem as electromechanical ice protection systems are based on resonant modes of the structure.

Acknowledgements This work has been partially funded by STAE foundation through the ReMOVEICE project and by ISAE-SUPAERO.

Declarations

Conflict of interest The authors declare that they have no conflict of interest.

Replication of results The algorithm is described in this paper together with numerical parameters. Numerical results are obtained with a 2D sequential code writing in Python and starting from scratch. The code implements mesh reading and writing, $\mathbb{P}_1$ finite element solver, filtering, objective and constraints evaluations, and sensitivities' computation. The external Python package NLOPT (Johnson 2014) is used for updating densities with MMA. Mesh generation is done with GMSH (Geuzaine and Remacle 2009) which provides MSH files to the code. Results are written in the VTK file format and are visualized with PARAVIEW (Ahrens et al. 2005).

References

Ahrens J, Geveci B, Law C (2005) Paraview: an end-user tool for large data visualization. The visualization handbook 717:8

Aircraft Icing Handbook. Civil Aviation Authority (2000)

Akl W, El-Sabbagh A, Al-Mitani K, Baz A (2009) Topology optimization of a plate coupled with acoustic cavity. Int J Solids Struct 46(10):2060–2074. https://doi.org/10.1016/j.ijsolstr.2008.05.034 (**Special Issue in Honor of Professor Liviu Librescu**)

Allaire G, Jouve F, Toader A-M (2004) Structural optimization using sensitivity analysis and a level-set method. J Comput Phys 194(1):363–393. https://doi.org/10.1016/j.jcp.2003.09.032

Amir O (2013) A topology optimization procedure for reinforced concrete structures. Comput Struct 114–115:46–58. https://doi.org/10.1016/j.compstruc.2012.10.011

Andreassen E, Clausen A, Schevenels M, Lazarov BS, Sigmund O (2011) Efficient topology optimization in matlab using 88 lines of code. Struct Multidisc Optim 43(1):1–16

Bennani L, Villedieu P, Salaun M (2016) A mixed adhesion-brittle fracture model and its application to the numerical study of ice shedding mechanisms. Eng Fract Mech 158:59–80. https://doi.org/10.1016/j.engfracmech.2016.02.050

Budinger M, Pommier-Budinger V, Napias G, Costa da Silva A (2016) Ultrasonic ice protection systems: analytical and numerical models for architecture tradeoff. J Aircraft 680–690. https://doi.org/10.2514/1.C033625

Budinger M, Pommier-Budinger V, Bennani L, Rouset P, Bonaccurso E, Dezitter F (2018) Electromechanical resonant ice protection systems: analysis of fracture propagation mechanisms. AIAA J 56(11):4412–4422. https://doi.org/10.2514/1.J056663

Budinger M, Pommier-Budinger V, Reysset A, Palanque V (2021) Electromechanical resonant ice protection systems: energetic and power considerations. AIAA J 59(7):2590–2602. https://doi.org/10.2514/1.J060008

Cao Y, Tan W, Wu Z (2018) Aircraft icing: an ongoing threat to aviation safety. Aerospace Sci Technol 75:353–385. https://doi.org/10.1016/j.ast.2017.12.028

Da D (2019). Topology optimization design of heterogeneous materials and structures. https://doi.org/10.1002/9781119687252

Da D, Yvonnet J (2020) Topology optimization for maximizing the fracture resistance of periodic quasi-brittle composites structures. Materials 13:15. https://doi.org/10.3390/ma13153279

Da D, Yvonnet J, Xia L, Li G (2018) Topology optimization of particle-matrix composites for optimal fracture resistance taking into account interfacial damage. Int J Numer Methods Eng 115(5):604–626

Dondl PW, Bhattacharya K (2016) Effective behavior of an interface propagating through a periodic elastic medium. Interfaces Free Boundaries 18(1):91–113

Duysinx P, Bendsøe MP (1998) Topology optimization of continuum structures with local stress constraints. Int J Numer Methods Eng 43(8):1453–1478

Frémond M (1987) Adhérence des solides. J Méc Théor Appl 6(3):383–407

Geuzaine C, Remacle J-F (2009) Gmsh: a 3-d finite element mesh generator with built-in pre-and post-processing facilities. Int J Numer Methods Eng 79(11):1309–1331

Griffith AA (1921) Vi the phenomena of rupture and flow in solids. Philos Trans R Soc Lond Ser A 221(582–593):163–198. https://doi.org/10.1098/rsta.1921.0006

Holmberg E, Torstenfelt B, Klarbring A (2013) Stress constrained topology optimization. Struct Multidisc Optim 48(1):33–47

Hsueh C-J, Bhattacharya K (2018) Optimizing microstructure for toughness: the model problem of peeling. Struct Multidisc Optim 58(3):1067–1080

Huang X, Xie Y-M (2010) A further review of eso type methods for topology optimization. Struct Multidisc Optim 41(5):671–683

Huang X, Zuo ZH, Xie YM (2010) Evolutionary topological optimization of vibrating continuum structures for natural frequencies. Comput Struct 88(5):357–364. https://doi.org/10.1016/j.compstruc.2009.11.011

Huang X, Tepylo N, Pommier-Budinger V, Budinger M, Bonaccurso E, Villedieu P, Bennani L (2019) A survey of icephobic coatings and their potential use in a hybrid coating/active ice protection system for aerospace applications. Progr Aerospace Sci 105:74–97. https://doi.org/10.1016/j.paerosci.2019.01.002

Johnson SG (2014) The NLopt nonlinear-optimization package. https://github.com/stevengj/nlopt

Kalkowski MK, Waters TP, Rustighi E (2015) Removing surface accretions with piezo-excited high-frequency structural waves. In: Active and Passive Smart Structures and Integrated Systems 2015, vol 9431, p 94311 . https://doi.org/10.1117/12.2087048. International Society for Optics and Photonics. https://www.spiedigitallibrary.org/conference-proceedings-of-spie/9431/94311T/Removing-surface-accretions-with-piezo-excited-high-frequency-structural-waves/10.1117/12.2087048.short

Kang Z, Pai L, Li M (2017) Topology optimization considering fracture mechanics behaviors at specified locations. Struct Multidisc Optim 55(5):1847–1864

Klarbring A, Torstenfelt B, Edlund U, Schmidt P, Simonsson K, Ansell H (2018) Minimizing crack energy release rate by topology optimization. Struct Multidisc Optim 58(4):1695–1703

Lazarov BS, Sigmund O (2011) Filters in topology optimization based on Helmholtz-type differential equations. Int J Numer Methods Eng 86(6):765–781

Le C, Norato J, Bruns T, Ha C, Tortorelli D (2010) Stress-based topology optimization for continua. Struct Multidisc Optim 41(4):605–620

Leary WM (2002) We freeze to please: a history of NASA's icing research tunnel and the quest for flight safety. Technical report. https://trid.trb.org/view/725075

Liu P, Luo Y, Kang Z (2016) Multi-material topology optimization considering interface behavior via xfem and level set method. Comput Methods Appl Mech Eng 308:113–133. https://doi.org/10.1016/j.cma.2016.05.016

Marbœuf A, Bennani L, Budinger M, Pommier-Budinger V (2020) Electromechanical resonant ice protection systems: numerical investigation through a phase-field mixed adhesive/brittle fracture model. Eng Fract Mech 230:106926. https://doi.org/10.1016/j.engfracmech.2020.106926

Martin E, Vandellos T, Leguillon D, Carrère N (2016) Initiation of edge debonding: coupled criterion versus cohesive zone model. Int J Fract 199(2):157–168

Mergel JC, Sauer RA, Saxena A (2014) Computational optimization of adhesive microstructures based on a nonlinear beam formulation. Struct Multidisc Optim 50:1001–1017

Miehe C, Hofacker M, Welschinger F (2010) A phase field model for rate-independent crack propagation: robust algorithmic implementation based on operator splits. Comput Methods Appl Mech Eng 199(45):2765–2778. https://doi.org/10.1016/j.cma.2010.04.011

Nguyen TT, Yvonnet J, Zhu Q-Z, Bornert M, Chateau C (2016) A phase-field method for computational modeling of interfacial damage interacting with crack propagation in realistic microstructures obtained by microtomography. Comput Methods Appl Mech Eng 312:567–595.

Niemann H, Morlier J, Shahdin A, Gourinat Y (2010) Damage localization using experimental modal parameters and topology optimization. Mech Syst Signal Process 24(3):636–652. https://doi.org/10.1016/j.ymssp.2009.10.022

Nishiwaki S, Frecker MI, Min S, Kikuchi N (1998) Topology optimization of compliant mechanisms using the homogenization method. Int J Numer Methods Eng 42(3):535–559

Overmeyer A, Palacios JL, Smith EC, Royer R (2011) Rotating testing of a low-power, non-thermal ultrasonic de-icing system for helicopter rotor blades. Technical report, SAE Technical Paper. https://www.sae.org/publications/technical-papers/content/2011-38-0098/

Overmeyer A, Palacios J, Smith E (2012) Actuator bonding optimization and system control of a rotor blade ultrasonic deicing system. In: 53rd AIAA/ASME/ASCE/AHS/ASC Structures, Structural Dynamics and Materials Conference 20th AIAA/ASME/AHS Adaptive Structures Conference 14th AIAA, p 1476. https://doi.org/10.2514/6.2012-1476

Palacios JL (2008) Design, fabrication, and testing of an ultrasonic de-icing system for helicopter rotor blades. PhD thesis, Pennsylvania State University, State College

Palacios J, Smith E (2005) Dynamic analysis and experimental testing of thin-walled structures driven by shear tube actuators. In: 46th AIAA/ASME/ASCE/AHS/ASC Structures, Structural Dynamics and Materials Conference, p 2112 . https://doi.org/10.2514/6.2005-2112

Palacios J, Smith E, Rose J et al (2008) Investigation of an ultrasonic ice protection system for helicopter rotor blades. In: Annual forum Proceedings-American Helicopter Society, vol 64, p 609. American Helicopter Society, Inc

Palacios J, Smith E, Rose J, Royer R (2011) Instantaneous de-icing of freezer ice via ultrasonic actuation. AIAA J 49(6):1158–1167. https://doi.org/10.2514/1.J050143

Palacios J, Smith E, Rose J, Royer R (2011) Ultrasonic de-icing of wind-tunnel impact icing. J Aircraft 48(3):1020–1027. https://doi.org/10.2514/1.C031201

Palanque V, Marbæuf A, Budinger M, Pommier-Budinger V, Bennani L (2021) Improving mechanical ice protection systems with substrate thickness and topology optimization. In preparation

Parks DM (1974) A stiffness derivative finite element technique for determination of crack tip stress intensity factors. Int J Fract 10(4):487–502

Pommier-Budinger V, Budinger M, Rouset P, Dezitter F, Huet F, Wetterwald M, Bonaccurso E (2018) Electromechanical resonant ice protection systems: initiation of fractures with piezoelectric actuators. AIAA J 56(11):4400–4411. https://doi.org/10.2514/1.J056662

Ramanathan S, Varadan VV, Varadan VK (2000) Deicing of helicopter blades using piezoelectric actuators. In: Smart Structures and Materials 2000: Smart Electronics and MEMS, vol 3990, pp 281–293. https://doi.org/10.1117/12.388906. International Society for Optics and Photonics. https://www.spiedigitallibrary.org/conference-proceedings-of-spie/3990/0000/Deicing-of-helicopter-blades-using-piezoelectric-actuators/10.1117/12.388906.short?SSO=1

Russ JB, Waisman H (2019) Topology optimization for brittle fracture resistance. Comput Methods Appl Mech Eng 347:238–263. https://doi.org/10.1016/j.cma.2018.12.031

Sigmund O (2001) A 99 line topology optimization code written in matlab. Struct Multidisc Optim 21(2):120–127

Sih G, Rice J (1965) Plane problems of cracks in dissimilar materials. J Appl Mech 32:418–423

Strobl T, Storm S, Thompson D, Hornung M, Thielecke F (2015) Feasibility study of a hybrid ice protection system. J Aircraft 52(6):2064–2076. https://doi.org/10.2514/1.C033161

Svanberg K (1987) The method of moving asymptotes-a new method for structural optimization. Int J Numer Methods Eng 24(2):359–373

Sylves K, Maute K, Dunn M (2009) Adhesive surface design using topology optimization. Struct Multidisc Optim 38:455–468

Venna SV, Lin Y- (2006) Mechatronic development of self-actuating in-flight deicing structures. IEEE/ASME Trans Mechatron 11(5):585–592. https://doi.org/10.1109/TMECH.2006.882990

Venna S, Lin Y-J, Botura G (2007) Piezoelectric transducer actuated leading edge de-icing with simultaneous shear and impulse forces. J Aircraft 44(2):509–515. https://doi.org/10.2514/1.23996

Venna S, Lin Y (2003) Development of self-actuating in-flight deicing structures with power consumption considerations. In: Proceedings of the American Society of Mechanical Engineers International Mechanical Engineering Congress and Exposition, pp 45–53. ASME Washington, DC

Villeneuve E, Harvey D, Zimcik D, Aubert R, Perron J (2015) Piezoelectric deicing system for rotorcraft. J Am Helicop Soc 60(4):1–12. https://doi.org/10.4050/JAHS.60.042001

Waisman H (2010) An analytical stiffness derivative extended finite element technique for extraction of crack tip strain energy release rates. Eng Fract Mech 77(16):3204–3215. https://doi.org/10.1016/j.engfracmech.2010.08.015

Work A, Lian Y (2018) A critical review of the measurement of ice adhesion to solid substrates. Progr Aerospace Sci 98:1–26. https://doi.org/10.1016/j.paerosci.2018.03.001

Wu J-Y (2017) A unified phase-field theory for the mechanics of damage and quasi-brittle failure. J Mech Phys Solids 103:72–99. https://doi.org/10.1016/j.jmps.2017.03.015

Wu J-Y, Nguyen VP (2018) A length scale insensitive phase-field damage model for brittle fracture. J Mech Phys Solids 119:20–42. https://doi.org/10.1016/j.jmps.2018.06.006

Xia L, Da D, Yvonnet J (2018) Topology optimization for maximizing the fracture resistance of quasi-brittle composites. Comput Methods Appl Mech Eng 332:234–254. https://doi.org/10.1016/j.cma.2017.12.021

Xia SM, Ponson L, Ravichandran G, Bhattacharya K (2015) Adhesion of heterogeneous thin films ii: Adhesive heterogeneity. J Mech Phys Solids 83:88–103. https://doi.org/10.1016/j.jmps.2015.06.010

Zargham S, Ward TA, Ramli R, Badruddin IA (2016) Topology optimization: a review for structural designs under vibration problems. Struct Multidisc Optim 53(6):1157–1177

Zhang Z, Chen B, Lu C, Wu H, Wu H, Jiang S, Chai G (2017) A novel thermo-mechanical anti-icing/de-icing system using bi-stable laminate composite structures with superhydrophobic surface. Compos Struct 180:933–943. https://doi.org/10.1016/j.compstruct.2017.08.068